

# Hadrontherapy

Dieter Schardt

**Abstract** In comparison to photon or electron beams used in conventional radiation therapy, high-energy proton- and heavy-ion beams offer favorable conditions for the treatment of deep-seated local tumors. Their physical depth-dose distribution in tissue is characterized by a small entrance dose and a distinct maximum (Bragg peak) near the end of range with a sharp fall-off at the distal edge. The well-defined range and the small lateral beam spread make it possible to deliver the dose with millimetre precision. Heavy ions, in addition, have an enhanced biological effectiveness in the Bragg peak region which is caused by the dense ionization and the resulting reduced cellular repair rate and make them very attractive for the treatment of radio-resistant local tumors. The article gives an introduction to hadrontherapy, including remarks on the history, basic physical and radiobiological principles, techniques of beam delivery and dose verification, and clinical experiences.

## 1 Introduction

Radiotherapy plays an important role in the treatment of cancer. Nowadays it is the most frequently and most successfully applied form of therapy after surgery and more than 50 % of all patients with localized malignant tumors are treated with radiation. In radiotherapy the key problem is to deliver the dose in such a way that ideally the intended target volume (covering the tumor region) receives 100 % of the planned dose needed to kill all cancer cells in the tumor, while the surrounding normal tissue does not receive any dose. This can not be achieved in practice because of the unavoidable dose deposited in the entrance channel of the irradiation, but in the past 60 years significant progress has been made to better understand the biological effectiveness of radiation and to improve the dose deposition towards the ideal and to increase thereby the tumor control rate for potentially curable cases.

---

D. Schardt (✉)

Biophysics Department, GSI Helmholtzzentrum für  
Schwerionenforschung GmbH, Planckstr. 1, 64291 Darmstadt, Germany  
e-mail: d.schardt@gsi.de

These achievements would not have been possible without the strong and fruitful interdisciplinary collaboration of scientists in the fields of oncology and radiation medicine, radiation biology, accelerator technology and engineering, as well as atomic and nuclear physics

The application of high-energy beams of **heavy charged particles** to radiotherapy was first considered in 1946 by Robert R. Wilson. He had worked in the Manhattan Project in Los Alamos and soon after the end of World war II decided to go back to Berkeley, where he found an inspiring academic research environment around Ernest Lawrence and collaborators. In the course of the design of a new cyclotron he started to investigate the range of 150 MeV protons and the stopping characteristics in various shielding materials. But, as he explains himself [53], he went on and studied the stopping characteristics in more detail and found "...the Bragg curve came up slowly and then came down very sharply which would make them very interesting for medical applications". In his classical paper entitled "*Radiological use of fast protons*" [51] he recognized the potential benefits of proton beams and predicted "...that precision exposures of well defined small volumes within the body will soon be feasible". Moreover he predicted that "...the intense specific ionization of alpha particles will make them the most desirable therapeutically" and "...heavier nuclei, such as very energetic carbon ions, may eventually become therapeutically practically".

Two years later the 184 in. synchrocyclotron at LBL Berkeley became available for experiments and the physical and radiobiological properties of proton beams were thoroughly investigated by Tobias and co-workers [46]. Patient treatments started in 1954 at LBL Berkeley, first with protons and later with helium beams. At the Harvard Cyclotron Lab (USA) more than 9000 patients were treated with proton beams (1961–2002), and also in Europe proton therapy begun in the 1950s and 1960s at laboratories in Uppsala (Sweden), Moscow and St. Petersburg.

Radiotherapy with heavier ions was initiated by Tobias and co-workers at the BEVALAC facility at LBL. Many interesting facts about the development of hadron-therapy can be found in [32]. At LBL most of the patient treatments (1975–1992) with heavy ions were performed with  $^{20}\text{Ne}$  ions (670 MeV/u) which at that time appeared to be most attractive because of their high relative biological effectiveness (RBE) combined with a low oxygen enhancement ratio (OER) in the treatment target volume (see e.g. Review articles [18, 30]). The beams were delivered to the patients by passive beam shaping systems, including scattering devices and wobbler magnets for broadening the beam and a number of passive elements like ridge filter, range modulator, collimator and bolus [5]. Until its closure in 1992 the BEVALAC was the only facility worldwide using heavy ions for the treatment of localized deep-seated tumors. In 1994 the heavy-ion medical accelerator HIMAC [11] dedicated to radiotherapy started with carbon ions at NIRS Chiba (Japan), using similar technical concepts as those pioneered at Berkeley. In Europe first treatments with  $^{12}\text{C}$  ions started at GSI Darmstadt in 1997.

It is amazing to see that Robert Wilson's predictions have all been verified. Besides the great success of using proton beams for cancer therapy, carbon ions have shown to be an effective treatment modality as high-LET radiation with more than 10,000

patients treated worldwide (mainly in Japan). Helium ions indeed seem to be therapeutically very promising as they offer a good compromise between high-LET and low-LET radiation, combined with favorable physical characteristics (much less scattering than protons). Clinical trials with He-ions are under preparation at the HIT facility in Heidelberg. At present only proton and carbon ion beams are used in hadrontherapy worldwide. The physical and radiobiological characteristics of these beams will be discussed in the next chapters.

## 2 Physical Characterization of Ion Beams in Radiotherapy

### 2.1 Depth-Dose Profile (Bragg Curve)

The major physical advantage of heavy charged particles as compared to photons is their characteristic depth-dose profile—the well known Bragg curve—named after Sir William Henry Bragg who investigated the energy deposition of  $\alpha$ -particles from a radium source in air at the beginning of the last century [2]. Whereas the photon dose decreases exponentially with penetration depth according to the absorption law for electromagnetic radiation, the depth-dose profile of heavy charged particles exhibits a flat plateau region with low dose and a distinct peak near to the end of range of the particles, the so-called ‘Bragg peak’ (Fig. 1).

This is a consequence of the interaction mechanism of the particles in the slowing-down process as described by the Bethe-formula which shows a  $1/\beta^2$  dependence of the specific energy loss  $dE/dx$ . The interaction of the projectiles (ions) with the absorbing medium is governed by inelastic collisions with the atomic electrons of the absorber material. At high velocities ( $\beta \equiv v/c$ ) the projectiles lose small amounts of energy in a large number of such collisions. The specific energy loss is at a maximum (Bragg peak) when the projectile reaches the Bohr velocity  $v_B = e^2/\hbar$ . This characteristic behavior of heavy charged particles was first investigated theoretically

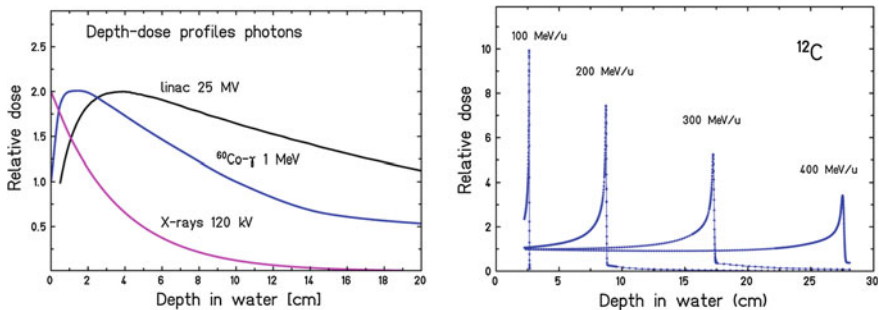


**Fig. 1** Comparison of depth-dose profiles in water for photons and high-energy carbon ions. The Bragg curves for <sup>12</sup>C ions were measured at GSI

by Niels Bohr by considering the energy loss per unit path length ( $dE/dx$ ) in a semi-classical treatment [3]. In the following only the basic steps are briefly sketched, more details can be found in the book *Experimental Nuclear Physics* by E. Segré. We consider an ion (projectile) with atomic number  $Z_p$  moving with velocity  $\vec{v}$  and at a distance  $r(t)$  of an atomic electron of the absorber. The Coulomb force acting between the ion and electron is given by

$$\left| \vec{F} \right| = \frac{Z_p \cdot e^2}{r^2} \quad (1)$$

assuming the electron to be free and at rest and a short interaction time (non-adiabatic conditions). For symmetry reasons only the vertical component of the momentum transfer to the electron has to be considered:

$$\Delta p_{\perp} = \int_{-\infty}^{\infty} F_{\perp} dt = \int_{-\infty}^{\infty} F_{\perp} \frac{dx}{v} \quad (2)$$

The integral can be solved using the Gaussian theorem, resulting in

$$\Delta p_{\perp} = \frac{2Z_p e^2}{b \cdot v}$$

where  $b$  denotes the impact parameter. The energy transferred to one electron is

$$\Delta E = \frac{(\Delta p_{\perp})^2}{2m_e} = \frac{2}{m_e} \cdot \left[ \frac{Z_p e^2}{bv} \right]^2 \quad (3)$$

From these relations it is clear that the transferred momentum and hence the energy loss of the ion gets large when the velocity is small, due to the longer interaction time.

Summing up the contributions of all interactions with atomic electrons by integration over the impact parameter from 0 to infinity leads to a divergent integral. Bohr solved this problem by replacing the boundaries by the limiting values  $b_{\min} = \hbar/(\gamma m_e v)$  and  $b_{\max} = \gamma \cdot v/\langle v \rangle$  resulting in the classical formula [3]:

$$-\frac{dE}{dx} = 4\pi \cdot n_e \cdot \frac{Z_p^2 e^4}{m_e v^2} \cdot \ln \left[ \frac{m_e v^2 \gamma^2}{\hbar \cdot \langle v \rangle} \right] \quad (4)$$

with  $\gamma$  the Lorentz factor and  $\hbar \cdot \langle v \rangle$  corresponding to the mean ionization potential  $I$  in the Bethe-formula (see (6)). The electron density  $n_e$  of the absorber material can be calculated by

$$n_e = \frac{N_A \cdot Z_T \cdot \rho}{A_T \cdot M_u} \quad (5)$$

with  $Z_T$ ,  $A_T$  and  $\rho$  denoting the atomic number, mass number and density of the absorber (target) material,  $N_A$  the Avogadro number and  $M_u$  the molar mass constant.

In 1930 Hans Bethe treated the problem quantum-mechanically and arrived in 1932 at the relativistic formula ('Bethe-Formula'):

$$-\frac{dE}{dx} = 4\pi \frac{Z_p^2 e^4}{m_e c^2 \beta^2} \cdot n_e \cdot \ln \left[ \frac{2m_e c^2 \beta^2}{I \cdot (1 - \beta^2)} \right] - \beta^2 \quad (6)$$

The specific energy loss  $dE/dx$  or 'stopping power' according to (6) is shown in Fig. 2 as a function of energy for protons and  $^{12}\text{C}$  ions passing through water.

Due to the  $1/\beta^2$  dependence the energy loss increases with decreasing particle energy. At high velocities the atomic electrons are completely stripped off and the projectile charge is equal to the atomic charge number  $Z_p$ . At lower velocities (for light ions below about 10 MeV/u), the mean charge state decreases due to the interplay of ionization and recombination processes and  $Z_p$  in (6) has to be replaced by the effective charge  $Z_{eff}$ , which can be described by the empirical Barkas-Formula [1]:

$$Z_{eff} = Z_p \cdot [1 - \exp(-125\beta \cdot Z_p^{-2/3})] \quad (7)$$

The maximum energy-loss rate, corresponding to the Bragg peak, is reached at a projectile velocity of

$$v_p \approx Z_p^{2/3} \cdot v_0 \quad (8)$$

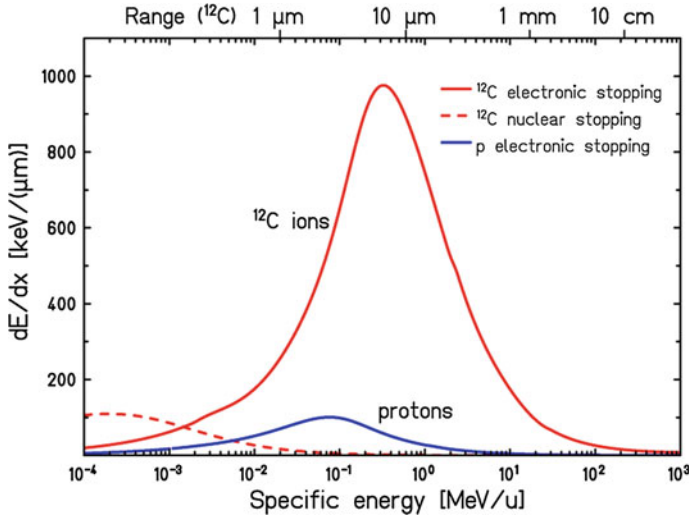


**Fig. 2** Specific electronic energy loss of protons and  $^{12}\text{C}$  ions in water. Note the logarithmic energy scale. The *dashed line* indicates the contribution of nuclear stopping. Residual ranges for  $^{12}\text{C}$  ions are given on the top

where  $v_0 = e^2/\hbar$  is the Bohr velocity and the corresponding  $\beta = e^2/(\hbar c) = 1/137$ . For  $^{12}\text{C}$  ions this maximum occurs at a specific energy of about 350 keV/u. At still lower projectile energies  $E_p < 10$  keV/u elastic collisions with target nuclei begin to contribute significantly to the energy loss and dominate the stopping process at the very end of the particle path (the last few  $\mu\text{m}$ ). The corresponding dose contribution is, however, very small and can be neglected here.

The dose deposited in tissue is the most important physical quantity in radiotherapy. It is defined by the term *absorbed dose* (unit Gray [Gy = J/kg]) as the mean energy  $d\varepsilon$  deposited by ionizing radiation in a mass element  $dm$  or volume element  $V$  with mass density  $\rho$ :

$$D = \frac{d\varepsilon}{dm} = \frac{1}{\rho} \frac{d\varepsilon}{dV} \quad (9)$$

For a parallel beam with particle fluence  $F$  the dose deposited in a thin slice of the absorber material can be written as:

$$D [\text{Gy}] = 1.6 \cdot 10^{-9} \cdot \frac{dE}{dx} \left[ \frac{\text{keV}}{\mu\text{m}} \right] \cdot F [\text{cm}^{-2}] \cdot \frac{1}{\rho} \left[ \frac{\text{cm}^3}{\text{g}} \right] \quad (10)$$

As an example, the energy deposition of a *single*  $^{12}\text{C}$  ion with an initial specific energy of 270 MeV/u as a function of depth in water is shown in Fig. 3 (dashed line), using the same data according to the Bethe-formula as in Fig. 2.

The energy deposition is characterized by a very sharp peak near the end of range of the ion, with a peak-to-entrance ratio of about 60. One has to keep in mind, however, that the energy loss along the penetration path is composed of a large

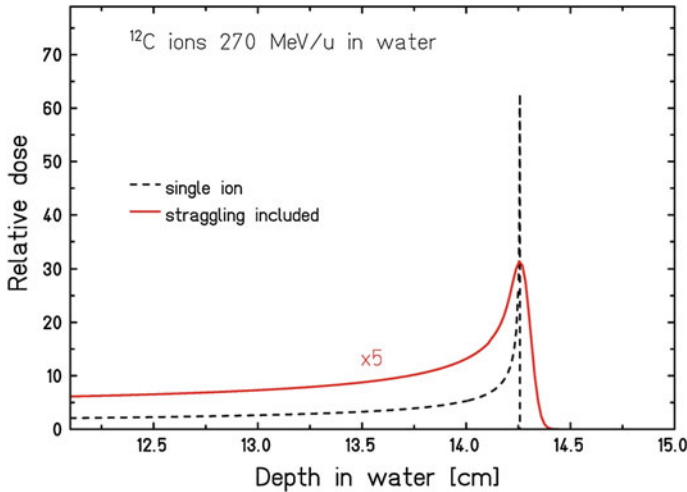


**Fig. 3** Energy deposition of 270 MeV/u  $^{12}\text{C}$  ions with a range of 14.25 cm in water for a *single ion* (dashed line) and an ion beam as used in therapy treatments (solid line)

number of single statistical processes. For an ion beam consisting of many ions (of the order of  $10^8$  or more) this leads to fluctuations in the energy loss and range for each individual ion, known as energy-loss-straggling and range-straggling. As a consequence, the extremely sharp peak of a single ion is smeared out and the peak-to-entrance ratio is significantly reduced (solid line in Fig. 3). This effect represents the main contribution for the observed width of the Bragg peak. Also the energy definition  $\Delta E/E$  of accelerated beams contributes to the width, but it is typically of the order of  $10^{-3}$  or better and can be noticed only at low energies where the straggling effects are smaller and the Bragg peaks may become very sharp.

The Bragg curve for a therapeutic ion beam shows an excellent dose profile (with a peak-to-entrance ratio of 5:1 in the example shown in Fig. 3) in comparison with the exponential dose fall-off for X-rays. This represents the major advantage of ion beams for the treatment of deep-seated local tumors.

## 2.2 Lateral Beam Spread

The lateral spread of proton or ion beams passing through an absorber is mainly caused by Coulomb scattering and is well described by the Molière-Theory [25]. For small angles the higher-order terms in Molière's solution can be neglected and the angular distribution can be approximated by a Gaussian function with a standard deviation given in [10]:

$$\sigma_{\theta}[\text{rad}] = \frac{14.1 \text{ MeV}}{\beta pc} \cdot Z_p \cdot \sqrt{d/L_{\text{rad}}} \cdot \left[ 1 + \frac{1}{9} \cdot \log_{10}(d/L_{\text{rad}}) \right] \quad (11)$$

The absorber material is characterized by the thickness  $d$  and the radiation length  $L_{\text{rad}}$ . Values of  $L_{\text{rad}}$  for common materials can be found in [47] and can be easily computed for compounds. In practice two different sources of angular beam spreading have to be considered: (a) scattering caused by materials in front of the patient (e.g., vacuum exit window, beam monitor, beam shaping devices) and (b) scattering in the patient's tissue between entrance point and stopping depth. The contributions of these two sources depend on the particle type and energy and are illustrated in Fig. 4 for a typical treatment beamline.

At low energies (a) represents the dominant contribution because even a small angular spread translates in a significant broadening of the beam spot due to the travelling distance of typically 0.5–1.0 m before entering the patient. This is critical in particular for protons. Therefore the material in the beam path in front of the patient should be kept as thin as possible, not contain heavy elements, and be located as close as possible towards the patient. At higher energies contribution (a) becomes less important or even negligible while (b) increases due to the larger penetration depths in tissue. Moreover, the calculations shown in Fig. 4 demonstrate the much smaller beam spread of  $^{12}\text{C}$  ions compared to protons. This allows a better dose conformation

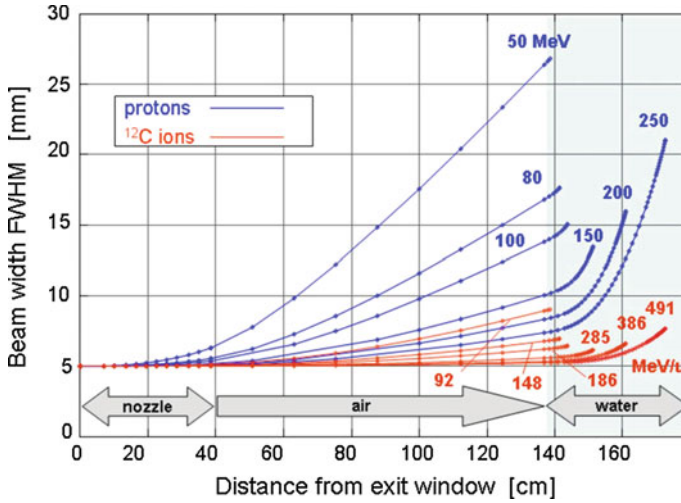


**Fig. 4** Calculated spread of proton and  $^{12}\text{C}$  ion beams in the nozzle, air gap and water (representing the patient's tissue) for a typical treatment beamline (U. Weber, GSI Darmstadt)

to the planned treatment volume (with a sharp dose fall-off at the boundaries) and is a special advantage for treating tumors located very near to critical organs.

### 2.3 Nuclear fragmentation

So far we considered the stopping of heavy charged particles in an absorber medium which is governed by inelastic collisions of the projectile with atomic electrons. However, also nuclear reactions along the penetration path may occur and cause a significant alteration of the radiation field. This holds in particular for heavier ions such as  $^{12}\text{C}$  which may break up (e.g. into three  $\alpha$ -particles) in nuclear reactions, producing thereby lighter fragments at high energies. Proton beams also get attenuated by nuclear reactions, leading amongst others to the production of secondary neutrons emitted mainly in forward direction. In the following we will consider the effects for heavy-ion beams in more detail.

At energies of several hundred MeV/u which are required for radiotherapy the most frequent nuclear interactions are peripheral collisions where the beam particles loose one or several nucleons. These reactions are well described by the so-called abrasion-ablation model according to [44] as illustrated in Fig. 5.

The total reaction cross sections at high energies ( $>100\text{MeV/u}$ ) can be well described by semi-empirical geometrical models and are almost constant over a wide energy range. Typical values (for water target) are about 350 mb for 200 MeV protons and 1400 mb for 380 MeV/u  $^{12}\text{C}$  ions. These values correspond to mean free



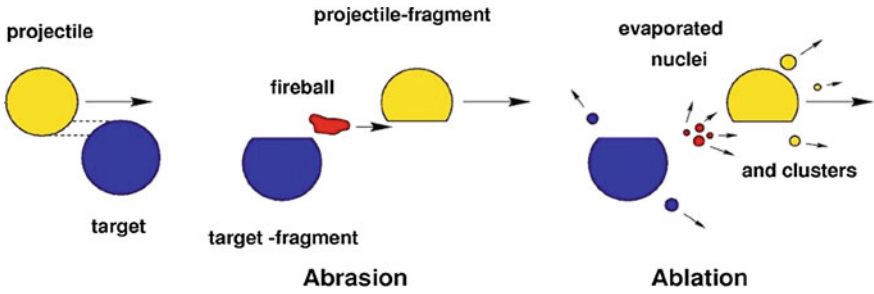


Fig. 5 Illustration of the Abrasion-ablation model [44]

path lengths in water of about 85 cm for protons and 21 cm for  $^{12}\text{C}$  ions. This means that e.g. at a depth of 10 cm in water about 11 % of the initial proton flux was lost by nuclear reactions, while this number is much higher (38 %) for  $^{12}\text{C}$  ions.

The projectile-fragments continue travelling with nearly the same velocity and direction. These nuclear reactions lead to an attenuation of the primary beam flux and a build-up of lower-Z fragments with increasing penetration depth. Recent experiments [9] at GSI studying the build-up functions of secondary charged particles were performed at  $^{12}\text{C}$  beam energies of 200 and 400 MeV/u, using a  $\Delta E - E$  scintillator telescope and time-of-flight (TOF) techniques. The experimental set-up is shown in Fig. 6.

In these experiments the nuclear charge  $Z_f$  of secondary fragments was identified by combining energy loss and time-of-flight (TOF) measurements (Fig. 7). Energy spectra and yields were recorded at lab angles of  $0^\circ - 10^\circ$  and at seven different water depths corresponding to the entrance channel, the Bragg peak region and the tail of the Bragg curve. The results include energy- and angular-distributions, fragment yields and attenuation of the primary carbon projectiles at all measured depths. As

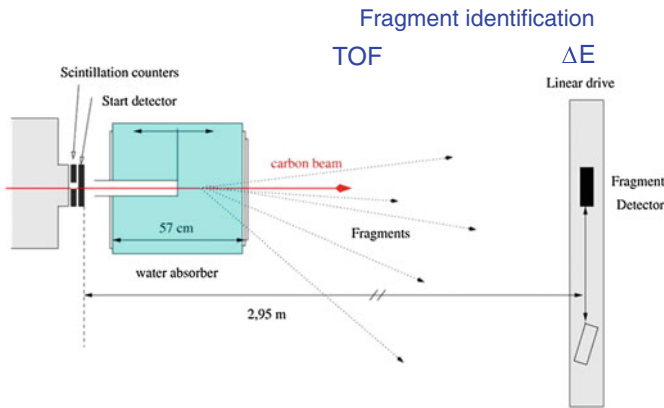
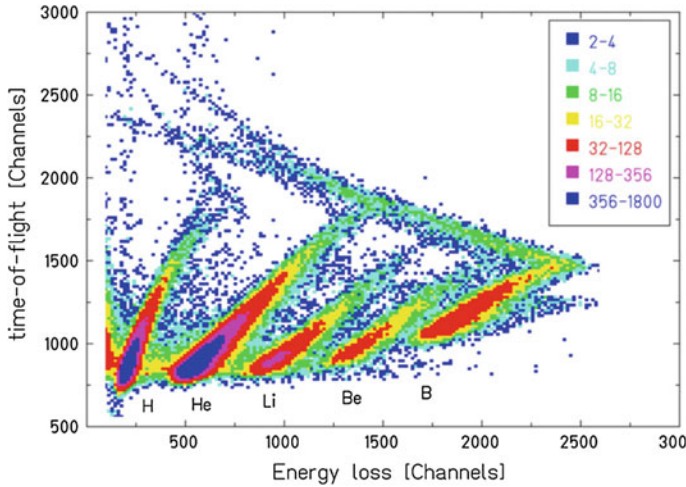
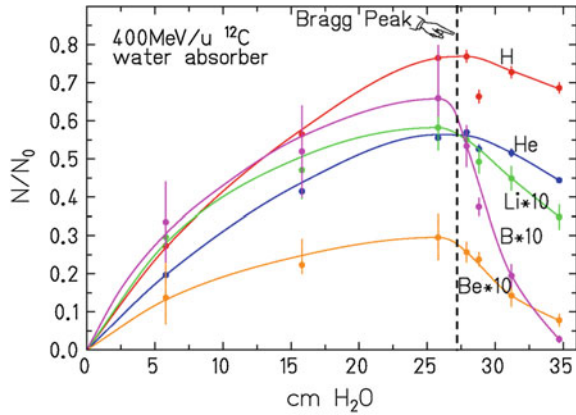


Fig. 6 Experimental setup for fragmentation measurements at GSI Darmstadt [9]



**Fig. 7** Two-dimensional scatter plot of time-of-flight versus energy loss from 400 MeV/u  $^{12}\text{C}$  ions fully stopped in a 31.1 cm thick water target. The detection angle was  $0^\circ$  with respect to the beam axis [9]

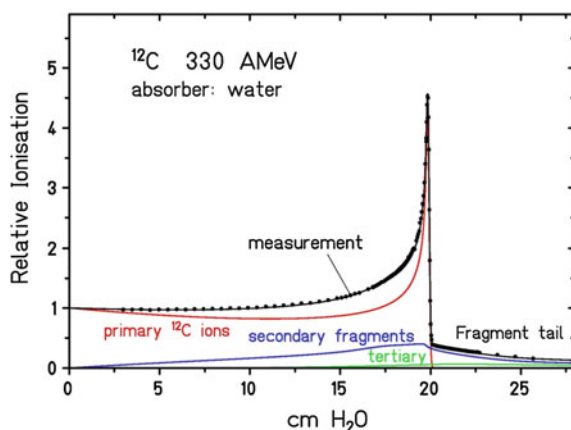
**Fig. 8** Build-up of secondary fragments in water. The data points were obtained by integration of the angular distributions measured at each depth [9]



an example, build-up functions and angular distributions for primary 400 MeV/u  $^{12}\text{C}$  ions passing through a water absorber of variable thickness are shown in Fig. 8.

As a consequence of nuclear fragmentation a rather complex radiation field is produced and leads to significant alterations which can also be observed in the shape of the Bragg curves. Since the range of the particles (at same velocity) scales with  $A/Z^2$  and therefore lower-charge fragments have a correspondingly longer range, the depth-dose profile of heavy-ion beams shows a characteristic fragment tail beyond the Bragg peak. The Bragg curve displayed in Fig. 9 for a 330 MeV/u  $^{12}\text{C}$  beam with the Bragg peak at about 20 cm depth of water exhibits a significant contribution of secondary fragments to the total dose. In the tail behind the Bragg peak first heavier fragments like B, Be, Li-ions contribute most of the dose, while the long range

**Fig. 9** Measured Bragg curve of 330 MeV/u  $^{12}\text{C}$  ions in water and calculated contributions of primary ions, secondary and tertiary nuclear fragments [45]



tail is caused essentially by protons and  $\alpha$ -particles. Of course, these fragmentation effects get more important with increasing depth due to the loss of primary ions and increasing production of fragments. The production of secondary fast neutrons was studied in detail by similar experiments using a  $\text{BaF}_2$  scintillation detector [7]. It was found that the number of neutrons per primary  $^{12}\text{C}$  ion stopping in water is  $0.54 \pm 20\%$ . Although this number is much higher compared to protons (0.025), the neutron doses are comparable and of the order of a few mSv per GyE delivered in the treatment. This is explained by the fact that a much higher number of protons (more than a factor 20) is needed to produce the same dose as carbon ions ( $Z^2$  factor in 6).

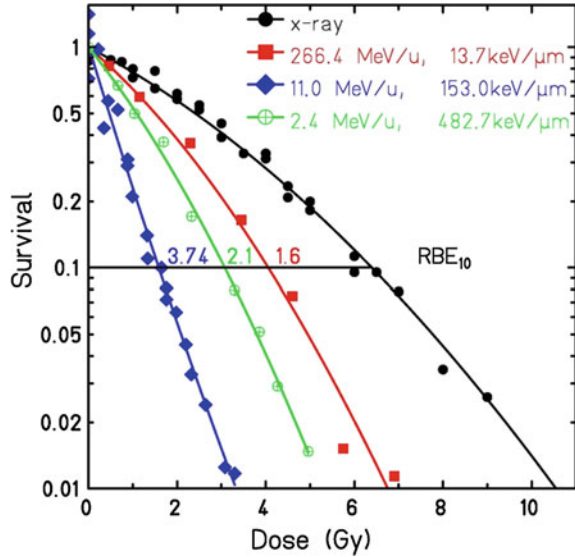
Concluding this chapter we can summarize the physical characteristics of heavy charged particles in radiotherapy as follows:

- The ‘inverted’ depth-dose profile (Bragg curve) of heavy charged particles offers excellent conditions for the treatment of deep-seated localized tumors
- The position in depth of the Bragg peak can be shifted by changing the kinetic energy of the particles and perfectly optimized to the treatment plan
- The lateral beam spread caused by Coulomb scattering is much smaller for heavy ions like  $^{12}\text{C}$  than for protons, especially for large penetration depths
- Nuclear fragmentation reactions lead to a complex radiation field in the patient’s tissue, especially for heavy ions, resulting in a characteristic dose tail beyond the Bragg peak. For protons such effects are much less significant.

### 3 Biological Effectiveness of Ion Beams

The effects of radiation on biological systems such as living cells have been investigated in innumerable radiobiological experiments since long time. In many of these studies the cell survival was measured as a function of the absorbed dose, defining

**Fig. 10** Experimental dose-effect curves of CHO-cells for irradiations with X-rays and  $^{12}\text{C}$  ions at different energies corresponding to different LET-values [52]



cell death as a complete loss of the proliferation capacity. The resulting dose-effect curves show characteristic slopes which can be understood in terms of the biological effectiveness of the applied radiation. As an example, survival curves of Chinese Hamster cells (CHO), a standard mammalian cell line, are shown in Fig. 10 for different types of radiation. The dose-effect curve for X-rays shows a non-linear behavior in form of a shoulder (survival  $S$  is plotted in log-scale vs. dose  $D$  in linear scale). At low doses the radio-sensitivity is small because most of the damage can be repaired. At higher doses the sensitivity increases and the slope of the curves decreases more and more steeply. This can be expressed by a linear-quadratic expression:

$$S = \exp(-\alpha D + \beta D^2) \quad (12)$$

where the coefficient  $\alpha$  describes the slope at small doses and gives the initially produced irreparable damage, and  $\beta$  the influence of repair which is important at higher doses. The ratio  $\alpha/\beta$  is therefore a measure for the repair capacity of the cells and takes typical values of 1–3 Gy for cells with high repair potential and close to 10 Gy for repair-deficient cells. For  $^{12}\text{C}$  ions the slope of the dose-effect curves depends strongly on the energy of the particles. At high energies the curves are steeper than the X-ray curve but still exhibit a small shoulder. At lower energies the survival curves become steeper, indicating a greater effectiveness of the particles. At an ion energy of 11 MeV/u the survival curve shows a purely exponential slope.

As a measure for the effectiveness the factor RBE (Relative Biological Effectiveness) was introduced as the ratio between X-ray dose and ion dose which are required to produce the same effect:

$$RBE = \frac{D_X}{D_{ion}} \Big|_{Isoeffect} \quad (13)$$

As can be seen from Fig. 10, the RBE values for  $^{12}\text{C}$  ions at 10% survival level increase from 1.6 at 266 MeV/u to 3.7 at 11 MeV/u. This behavior can be easily understood in terms of the energy-LET relation (Bethe-Formula), i.e. at low energies (near the Bragg peak) the local energy deposition and hence the irreparable damage are much higher than at high energies. Surprisingly, at still lower ion energies RBE does not further increase but decreases again (see data for 2.1 MeV/u). This can be explained by two different effects: (1) if the dose deposited by a single ion is much higher than necessary to kill the cell, the energy is wasted and leads to a saturation effect ('overkill'), and (2) at very low energy, i.e. high LET, the fluences required for doses of a few Gy become very small (see 10) and a certain fraction of the cells may not be hit at all, thus again decreasing the effectiveness.

Since the discovery of the DNA and the genetic code in 1953 it became clear that the DNA molecule in the cell nucleus represents the sensitive radiation target. The existence of genes as a unit of heredity inside of cells was known long before from biological experiments which showed radiation-induced mutation in flies. These results had attracted also the interest of physicists like Max Delbrück, who had suggested already in 1935 the nature of genes as macromolecules, and Erwin Schrödinger following these ideas in his famous lecture "What is life?" [40].

Various possible damages of the DNA are schematically illustrated in Fig. 11. The most critical lesion is the double strand break which leads to cell death or mis-repair

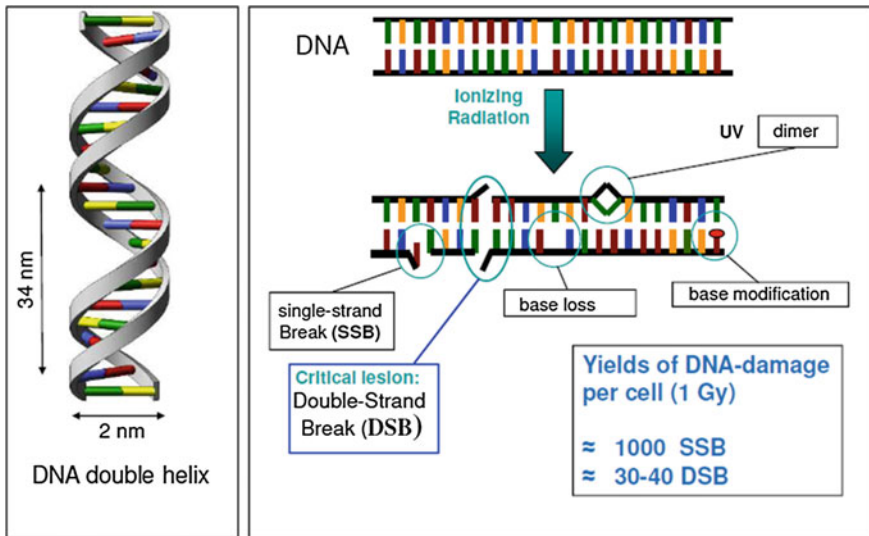


Fig. 11 DNA-damage induced by ionizing radiation [37]

and cancerogenesis. The yields of DNA-damage are rough estimates illustrating the order of magnitude [37].

The higher biological effectiveness of ion beams can be explained by the microscopic structure of particle tracks and their interaction with the DNA molecule. As discussed above, the interaction of energetic ions with the tissue is governed by inelastic collisions with the atomic electrons. Since the ion/electron mass ratio is very large, the ions are moving on practically straight trajectories through the tissue. Delta-electrons are emitted mainly in forward direction and those emitted at larger angles have comparatively low energies and short ranges (due to the collision kinematics). The *local* dose inside these particle ‘tracks’ can reach values up to a few thousand Gy, but decreases extremely steeply ( $\sim 1/r^2$ ) with the radial distance  $r$  down to the order of 1 Gy at about 1  $\mu\text{m}$ . This means that the dose deposition of an ion passing through a cell is highly concentrated in the track core whereas other regions of the cell do not receive any dose. This is in contrast to the dose deposition of sparsely ionizing radiation like photons or electrons, where the dose deposition is almost homogeneous in the region of a cell because it is the result of many ionizing events which are statistically distributed over the whole volume.

For fast protons the local  $\delta$ -electron density along their tracks is relatively small, their biological effectiveness is not very different from photons (RBE close to 1). For  $^{12}\text{C}$  ions, due to the  $Z^2$  factor in the Bethe-formula, the local dose deposition and ionization density is much higher, especially at low energies near the Bragg peak. This is illustrated in Fig. 12 by Monte-Carlo simulations [19] showing the trajectories of individual  $\delta$ -electrons of protons and  $^{12}\text{C}$  ions at various energies. While proton irradiation leads mostly to repairable DNA-damage, the probability for multiple damage of the DNA molecule (double strand breaks) and cell death is much higher for  $^{12}\text{C}$  ions, especially at the end of their track.

The elevated biological effectiveness of ion beams is of greatest importance for therapy applications and has to be correctly implemented into the treatment planning procedures. The fact that RBE depends on many different parameters such as the biological end point, dose, particle type, and energy, composition of the radiation field as well as the tissue under consideration poses however a big challenge. Therefore RBE-values are different for every location in the treatment volume. This is most important when the radiation dose is applied by beam scanning and the RBE varies from pixel to pixel. At GSI Darmstadt a model was developed for calculating the RBE value at any position in the irradiation field. The so-called Local Effect Model (LEM) [38, 39] relates the response of biological systems following ion irradiation to the corresponding response after photon irradiation. It assumes that the biological effect of irradiation is entirely determined by the spatial local dose distribution inside the cell nucleus. The basic principle is to convolute the radial dose distribution of the ion tracks with the non-linear photon dose effect curve (Fig. 13).

The accumulated local dose in the cell nucleus from different ion tracks is calculated for small sub-volumes individually using a track structure model. With knowledge of the deposited dose, the resulting biological damage is extrapolated from data of photon experiments for each sub-volume and integrated over the entire cell nucleus. This procedure was implemented into the treatment planning code TRiP

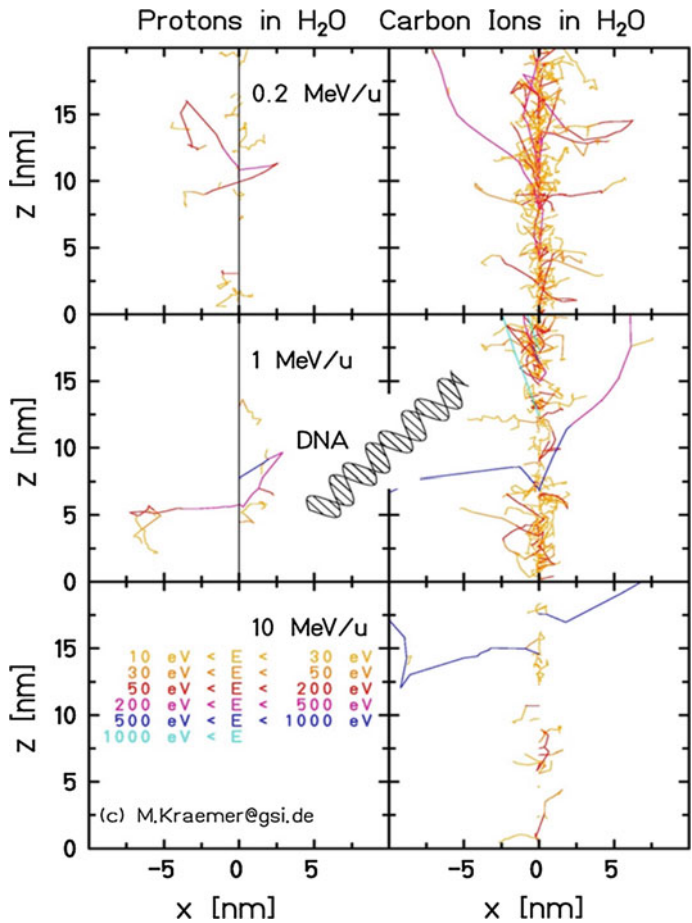


**Fig. 12** Monte-Carlo simulations [19] showing individual tracks of  $\delta$ -electrons produced by energetic protons and  $^{12}\text{C}$  ions penetrating tissue. The particles enter at  $x = 0$  and move along the  $z$ -axis

[20] which was successfully applied for the preparation of treatment plans for all patients treated within the pilot project at GSI.

Concluding this chapter we can state that heavy ions like  $^{12}\text{C}$ , besides their favorable depth-dose profile, exhibit an elevated biological effectiveness (or cell killing power) which represents an important advantage for the treatment of radio-resistant tumors. The biological effectiveness generally increases with the atomic number  $Z$  of the projectile and is much higher in the Bragg peak region than in the entrance channel. In numerous radiobiological investigations carried out over the last decades it has been found that  $^{12}\text{C}$  ions seem to be a good compromise with respect to the biological effectiveness in the tumor volume and with acceptable tolerance of the normal tissue which has to be traversed. These findings were confirmed already by



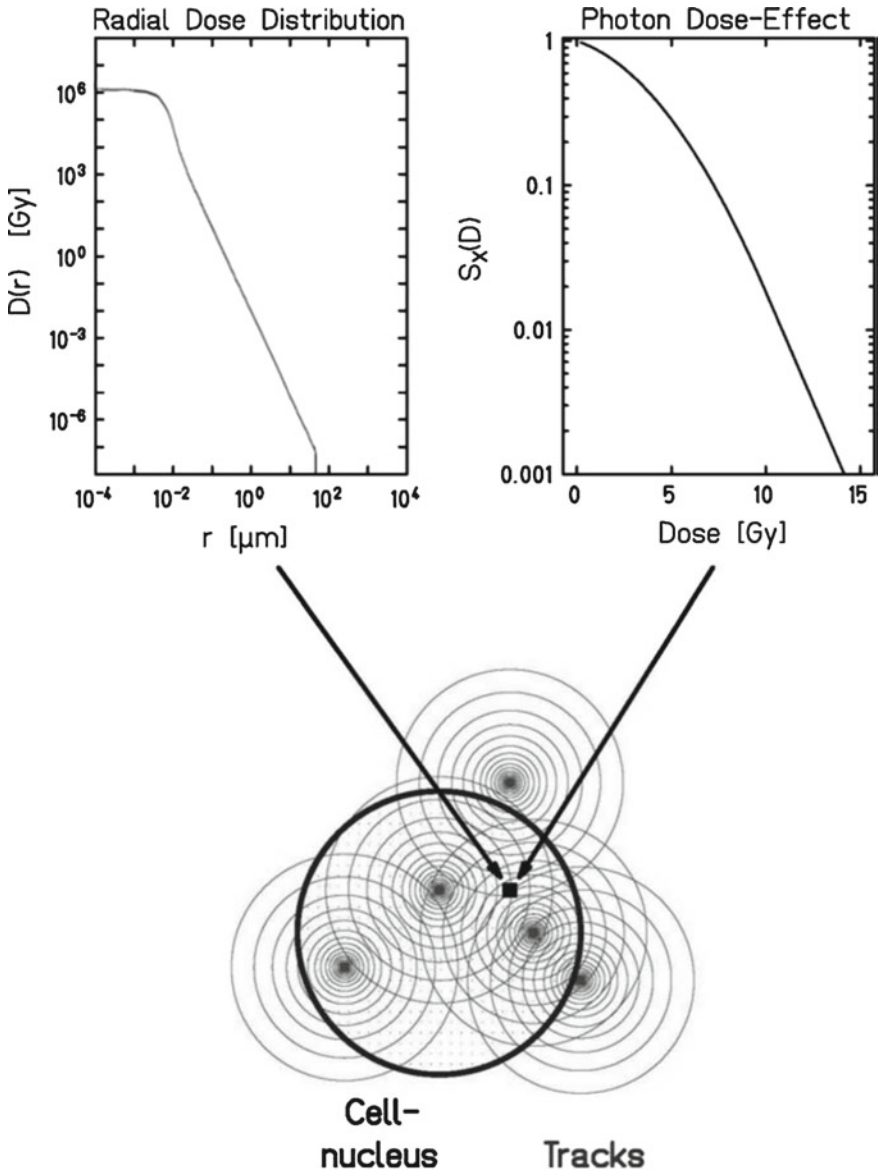


**Fig. 13** Principle of the Local Effect Model (LEM) [38]

the first  $^{12}\text{C}$  ion treatments within the pilot project (1993–2008) at GSI, where 440 patients, most of them with radio-resistant tumors in the skull base, were successfully treated with tumor control rates up to 90 % [43]. A number of new clinical studies currently being performed at the clinical center HIT (Heidelberg/Germany)



show promising results, see e.g. [14]. Moreover, the HIT facility offers the unique possibility to perform both proton and  $^{12}\text{C}$  ion treatments under the same (technical) irradiation conditions, using a beam scanning delivery system for delivering a highly tumor-conform dose deposition.

## 4 Accelerators and Beam Delivery Systems

Proton and ion beam therapy require powerful accelerators in order to reach clinically relevant particle ranges in tissue up to 30 cm. The range of ions with the same specific energy (in MeV/u) scales with the factor  $A/Z^2$ . For protons and He-ions energies up to 250 MeV/u are required, for  $^{12}\text{C}$  ions 430 MeV/u, for heavier ions like  $^{16}\text{O}$  more than 500 MeV/u (Fig. 14). These energies correspond to magnetic rigidities  $B\rho$  of 2.3 Tm for protons and 6.6 Tm for  $^{12}\text{C}$  ions.

Today most therapy facilities offering exclusively protons are operated with cyclotrons, while all facilities with  $^{12}\text{C}$  ions are using synchrotron accelerators. Cyclotrons are considered as easy to operate, highly reliable, and compact machines. They offer continuous beam (ideal for beam scanning) and extremely stable and regulable intensities, but no energy variation, i.e. only by means of passive degraders in the beam line. Synchrotrons, on the other hand, offer fast energy variation (from pulse to pulse), but need an injector and a delicate extraction system and are more complex in operation.

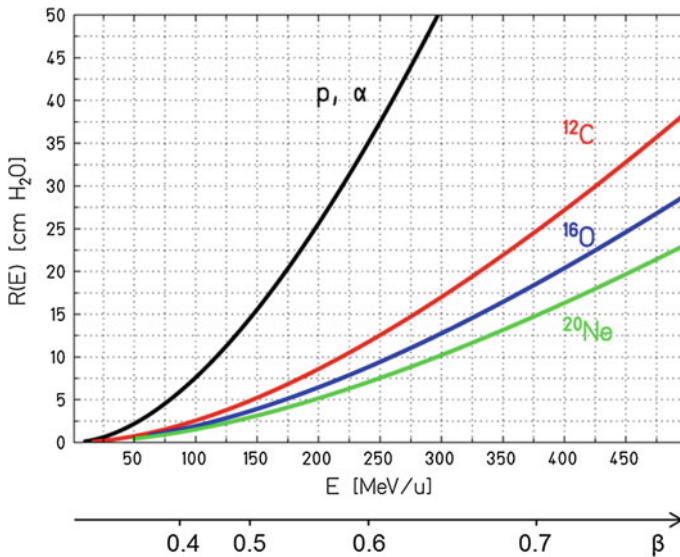


**Fig. 14** Range-energy relation and velocity  $\beta = v/c$  for protons and light ions in water

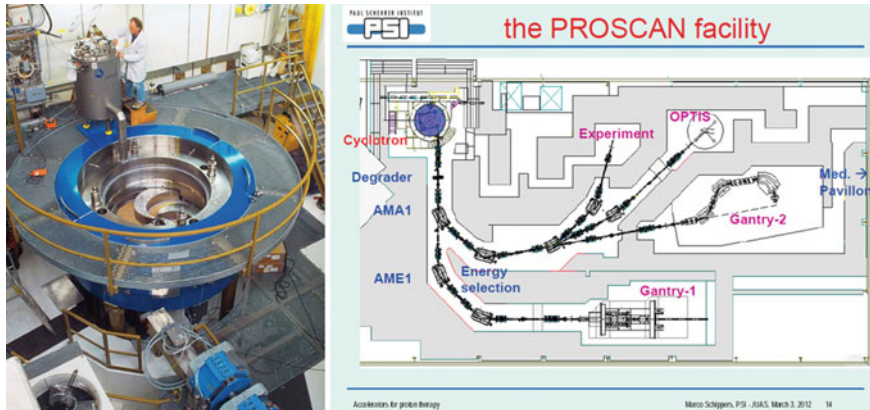


**Fig. 15** Layout of the PROSCAN-Facility at PSI in Villigen (Switzerland). The left part shows the super-conducting cyclotron during maintenance [35]

Super-conducting cyclotrons (only 2–3 m in diameter) need very little floor space and are thus ideally suited for integration in the hospital. As an example the layout of the proton therapy facility PROSCAN is shown in Fig. 15. Fast energy variation required for the spot-scanning technique is accomplished here with a carbon wedge degrader system followed by a cleaning and analyzing section, accepting however significant beam losses and related activation problems. By this arrangement fast neutrons produced in the degrader and emerging mainly in forward direction do not reach the patient treatment area. The treatment beam is sent to two Gantry systems and delivered by the spot-scanning techniques developed at PSI.

The synchrotron solution was chosen for all heavy-ion therapy centres presently in operation or under construction. Nonetheless, there are ongoing efforts for the design of cyclotrons for heavy-ion therapy as well. The problem of the higher magnetic rigidities for heavy ions might be overcome by superconducting cyclotrons. Compact accelerators for modern carbon-ion therapy centres such as the HIBMC Hyogo, Japan (designed by Mitsubishi) or Heidelberg Ion Therapy centre (HIT) Heidelberg, Germany (GSI Design) combine injection linacs less than 10 m long with synchrotron rings of 20–30 m diameter.

Particle beams provided by cyclotron or synchrotron accelerators are typically narrow, pencil-like beams centred at the axis of the beam tube. An important task which is performed by the so-called beam delivery system is to distribute the beam over the planned target volume (PTV) accurately and homogeneously with the desired dose distribution. Two different basic strategies were followed which in their extreme forms are represented by (i) the fully passive systems with fixed beam modulation or (ii) the fully active beam scanning systems. In the first case, the particle beam is adapted in three dimensions to the target volume only by passive non-variable field shaping elements. In the second case, the target volume is dissected in small volume elements (voxels) and a fine pencil-like beam is used to fill the voxels with the

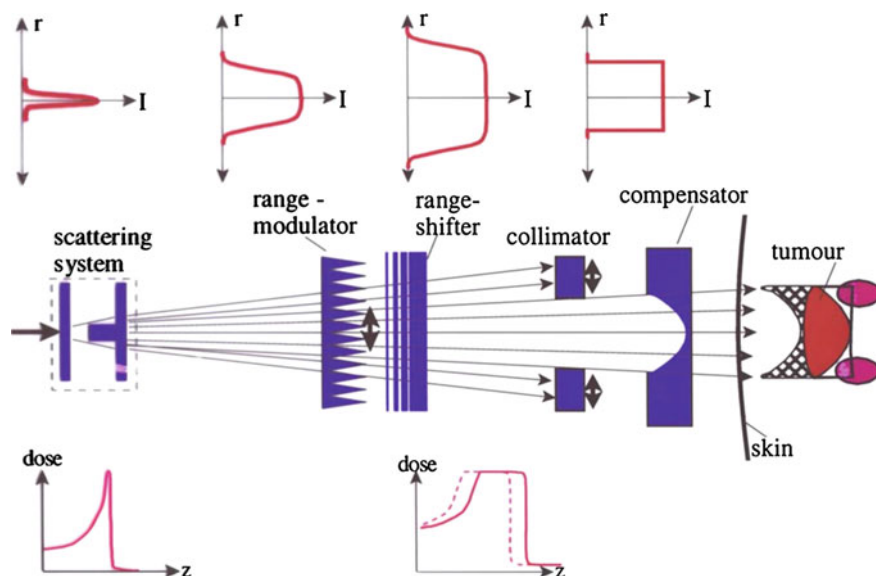
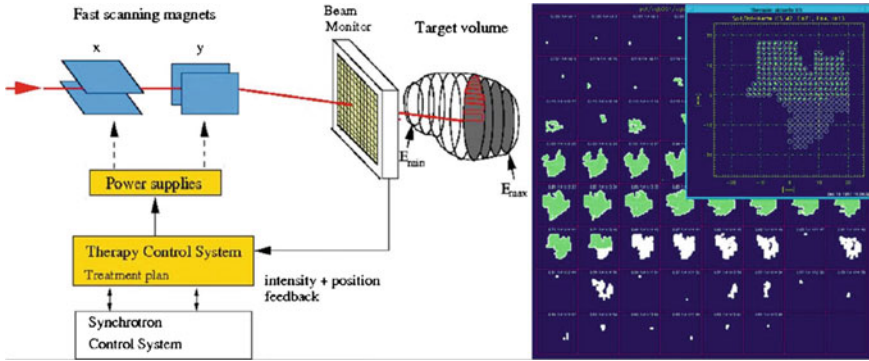


Fig. 16 Principle of fully passive beam delivery system (see e.g. [5])

appropriate dose, ideally without any material in the beam path. Many other solutions in between these two extremes are possible and were discussed in [5]. The principle of a fully passive system is shown in Fig. 16. The initially narrow beam delivered by the accelerator is first broadened by a scattering device, normally a double-scattering system which generates a flat transversal profile in a most efficient way. The pristine Bragg peak is spread out by a range modulator in order to cover the entire length of the target volume. The whole spread-out Bragg peak (SOBP) can be shifted in depth by absorber plates (range shifter). The following two devices are patient specific and need to be precisely fabricated: the collimator cuts out the field area defined by the largest target contour as seen in beam's eye view, preventing particles outside the field to pass through. The range compensator adjusts the distal depth pattern, taking into account also the complex tissue composition. A major limitation of the fully passive modulation system is the fixed width of the SOBP, which may result in significant dose deposition outside the target volume, e.g. in the proximal part when the particle range is adjusted to the distal contours (as shown in Fig. 16).

In the early 1990s a new beam delivery technique was developed almost in parallel at PSI (Switzerland) and at GSI (Germany). Both the spot scanning system (PSI) [29] and the raster scanning system (GSI) [8] represent fully active techniques in the sense that no passive elements are used in order to adapt the dose deposition optimally to the target volume. The basic principle of the raster scanning system is shown in Fig. 17. In contrast to the passive systems there is no scattering device, but the fine pencil-like beam is moved in horizontal and vertical direction by fast magnetic deflection magnets. The treatment dose is delivered slice by slice, each slice corresponding to



**Fig. 17** Principle of the intensity-controlled raster scanning system at GSI [8]. The position of the beam and the number of ions (corresponding to the dose) are recorded in real-time by large-area parallel-plate ion chambers and multi-wire chambers

constant beam energy. The scan path within one slice follows a meander-like line connecting all points of a dense grid. The spacing between adjacent raster points is typically 2 mm and much smaller than the beam-spot. This makes the system more robust since many grid points contribute to the covering of a small area.

When the desired dose in one voxel is reached (this is controlled by the beam monitor system in front of the patient), the beam is moved to the next voxel. After completion of one slice the synchrotron beam extraction is instantly interrupted and the beam energy for the next slice is selected and delivered with the next synchrotron pulse. The scanning control system is linked with the accelerator control system and requests the appropriate beam parameters for each slice irradiation during execution of the treatment plan. With this system it is possible to adapt the dose distribution to any complex shape of the target volume, individually for each patient and without any patient-specific hardware.

## 5 Treatment Planning

The first step of treatment planning for any radiation therapy modality is to define and delineate the target volume on the basis of modern imaging techniques. X-ray CT provides quantitative information about the anatomical structures by recording photon attenuation images with a typical pixel resolution of 1 mm and slice thickness of 3 mm. Native CT data (without contrast agents) are essential for calculating the particle range and dose deposited in tissue and have to be recorded under the same conditions and with the same fixation aids (e.g. head mask) as used later in the treatment. Magnetic resonance imaging (MRI) and Positron-Emission-Tomography (PET) are often applied in combination with CT to allow for a better definition of the target volume and organs at risk.

The following steps of preparation are needed before the treatment can start:

- definition and delineation of the target volume (CT, MRI, PET)
- transformation of patient CT-data to water-equivalent path-length of ions
- Treatment planning:
  - find best entrance ports
  - optimization of absorbed dose [Gy] based on physical model
  - heavy ions: biological optimization (incl. RBE, biol. model)
- Verification of planned dose distribution in water phantom
- Patient positioning/verification
- Irradiation.

To calculate the dose deposition including the exact position of the Bragg peak in heterogeneous tissue, the relationship between CT numbers (given in Hounsfield units) and stopping power has to be established. The concept of water-equivalent path length (WEPL) is used to relate the traversal of an ion through a given CT voxel to the corresponding ion path length in water. There is no simple functional relationship between CT number and stopping power or WEPL, but in a first step it can be approximated by linear sections. The CT-WEPL relationship has been carefully investigated and verified experimentally by measuring pairs of CT numbers and stopping powers for animal tissue samples [23, 33, 34].

For passive beam delivery systems, treatment planning is equivalent in optimizing a set of beam shaping elements and preparing patient-specific hardware for each individual case [5]. It is a major advantage of fully active scanning beam devices that patient-specific beam shaping elements are not needed at all. Since the pristine Bragg peaks are relatively narrow, the irradiation of extended target volumes requires the superposition of a number of Bragg curves in order to move the position of the Bragg peak in depth over the whole target volume (Fig. 18). With passive delivery systems this is achieved by range shifters and ridge-filters located in front of the patient, while scanning systems can be combined with an active energy variation by the accelerator control system.

For protons the optimization commonly is restricted to absorbed dose only, applying a constant RBE value of 1.0–1.1 [12, 26], but the need of better consideration of RBE for protons is still under discussion [16]. For heavy-ion therapy the biological effective dose has to be optimized, which is a difficult task in view of the manifold dependencies of RBE and the complex radiation field. Considering the fact that RBE increases significantly towards the end of range of the ions, the absorbed dose has to be lowered correspondingly in order to obtain a uniform biological effective dose over the planned target volume (see Fig. 19). For passive delivery systems this requires patient-specific complex beam shaping elements such as rotating propellers in order to modulate the SOBP.

A major improvement was achieved by the development of intensity-modulated particle therapy (IMPT), using beam scanning techniques (see above), where the target volume is irradiated point by point. With such systems any prescribed dose can be assigned to each voxel separately. This was a prerequisite for the development of

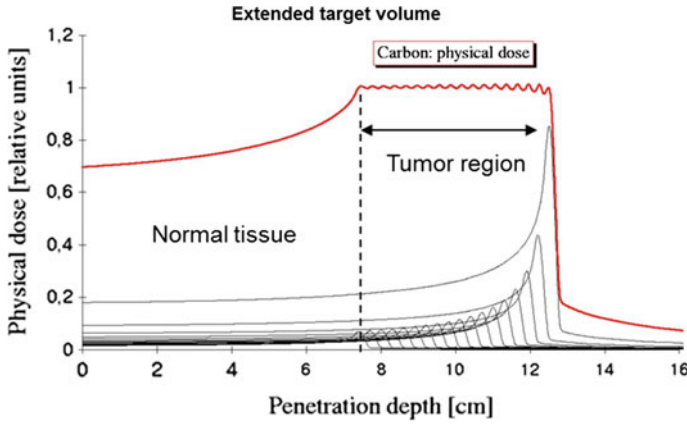


**Fig. 18** Superposition of Bragg curves for the irradiation of an extended target volume with constant dose (M. Krämer, U. Weber GSI)

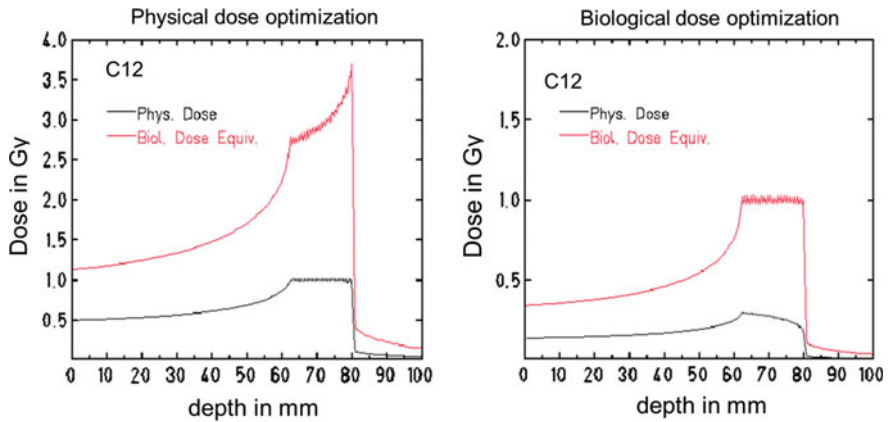


**Fig. 19** Correspondence of absorbed dose for 1 Gy physical dose (*left*) and 1 Gy (RBE) biological effective dose in a planned target volume at 60–80 mm in depth (M. Krämer GSI)

the *Biological Treatment Planning System* (TRiP) for  $^{12}\text{C}$  ions at GSI Darmstadt [20, 21]. Using the Local Effect Model (LEM), the local RBE can be calculated for any position in the treatment volume. However, this requires not only knowledge of the absorbed dose at each position (voxel), but also the composition of the radiation field at each point, since RBE depends on LET which in turn depends on the characteristics of the particle field. The latter information (e.g. the energy spectra of the primary  $^{12}\text{C}$  ions, secondary fragment yields, energy spectra and angular distributions) has to be provided by a physical model characterizing the beam and its interaction with tissue. The first step then is an optimization of the absorbed dose (physical dose) in order to reach highest conformation of the treatment dose to the planned target volume (PTV). In a second step, the biological optimization is performed by a complex iteration



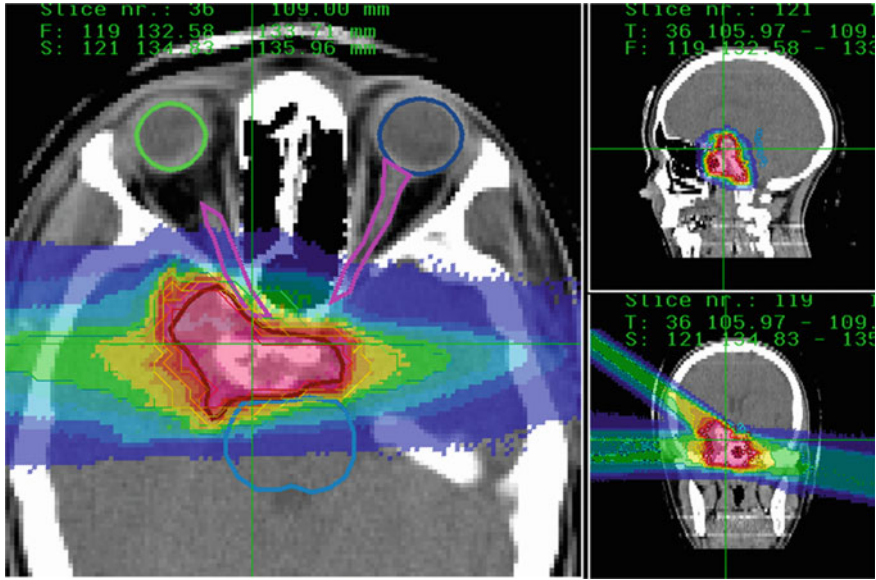


**Fig. 20** Biologically effective dose distribution optimized with the treatment planning system TRiP [20] for a skull base tumor treated at GSI Darmstadt. With three fields an excellent sparing of critical organs (brain stem and optical nerves) is achieved. (Figure courtesy of O. Jäkel, DKFZ Heidelberg)

procedure, which finally results in a uniform deposition of the desired biologically effective dose over the PTV and produces all machine settings for the accelerator control and scanning system. The treatment plan shown in Fig. 20 represents a typical case of skull base tumors treated at GSI and illustrates the dose conformation and the sparing of organs at risk (here the brain stem and the optic nerves). The treatment planning system TRiP in combination with the planning software ‘Voxelplan’ (DKFZ Heidelberg), was routinely used for carbon-ion treatments during 1997–2008 and has proven to be a reliable tool for heavy-ion therapy with scanning beams.

## 6 Dose Verification Techniques

Verification of the absolute dose and the spatial dose distribution in a phantom prior to the patient treatment is an important part of quality assurance (QA). In conventional radiotherapy with photon or electron beams this is routinely performed using small air-filled ion chambers and a standard water phantom. The same techniques can be applied to proton or heavy ion beams. The dose to water can be written as

$$D_w(P_{eff}) = M_{corr} \cdot N_{w,Co60} \cdot k_Q \quad (14)$$

where  $P_{eff}$  denotes the effective point of measurement, i.e., the point in depth to which the measured dose refers,  $M_{corr}$  is the measured charge in the air cavity corrected for deviations from the reference conditions,  $N_{w,Co60}$  is the  $^{60}\text{Co}$  calibration factor, and  $k_Q$  is a calculated beam quality correction factor which takes into account the stopping power ratios of water to air and specific correction factors for charged particles.

In static irradiation fields the dose distribution can be verified by moving a single small ion chamber successively to different locations in the water phantom. Dose measurements with a single ionization chamber placed in a water phantom would, however, be ineffective for scanning systems, as each measurement would require repeated complete applications of the treatment field. Instead dedicated systems were developed, consisting of many ion chambers mounted in a block structure, which permits to measure the dose at many different locations simultaneously [17]. For further details about dosimetry techniques for proton and ion beams see e.g. [13, 36].

The biological effective dose, however, can only be verified in radiobiological measurements with living cells. For this purpose, numerous cell survival experiments with a mammalian cell line (CHO) have been carried out at GSI Darmstadt. The cells were irradiated in a therapy-like scenario using a cylindrical head phantom, which allowed to place the cell cultures at selected positions in 3 dimensions.

These measurements confirmed the validity of the LEM and its applicability for complex target volumes with surrounding organs at risk. The example shown in Fig. 21 demonstrates the good agreement of the measured cell survival data with the prediction of the biological planning with TRiP, including the LEM calculations. As explained above the constant biological effect in the planned target volume is obtained by decreasing the physical dose towards the distal zone.

## 6.1 *In-vivo treatment monitoring*

Radiation therapy with heavy ions such as  $^{12}\text{C}$  or  $^{16}\text{O}$  offers the unique possibility of in-vivo monitoring of the treatment irradiation. This yields an independent experimental verification of correct treatment planning and beam delivery, especially the monitoring of the ion ranges in tissue which is invaluable for treating tumors near critical structures. The principle of the measurement is sketched in Fig. 22.

Along the penetration path in tissue a small fraction of the primary  $^{12}\text{C}$  ions undergoes a peripheral nuclear reaction and continues travelling as  $^{11}\text{C}$  fragment with about the same velocity (c.f. Fig. 5). As they have the same nuclear charge they reach almost the same depth as the primary ions ( $^{11}\text{C}$  ions have a little shorter range than  $^{12}\text{C}$  because of the lower mass number). The spatial distribution of the  $\beta^+$ -activity of the  $^{11}\text{C}$  ions can be obtained by coincident recording of the annihilation radiation in two opposite detector heads and applying tomographic reconstruction algorithms. The  $\beta^+$ -activity distribution is then compared to the expected distribution which is calculated based on the patient CT-data, the treatment plan and the actual



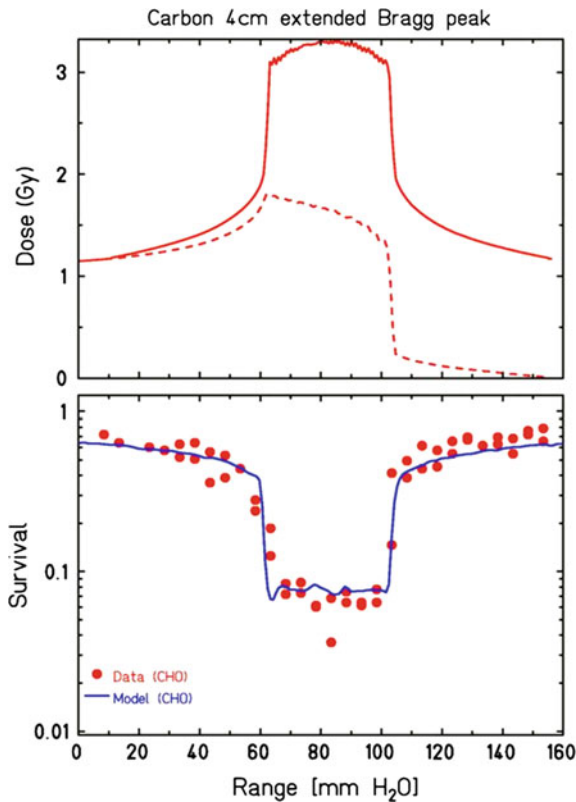


**Fig. 21** Biological verification of a treatment plan with two opposing fields of  $^{12}\text{C}$  ions calculated with the treatment planning code TRiP (solid line). The profiles of the two fields were optimized in order to obtain a constant biological effect at 80–100 mm depths in water. This was verified experimentally by cell survival measurements (data points) [22]

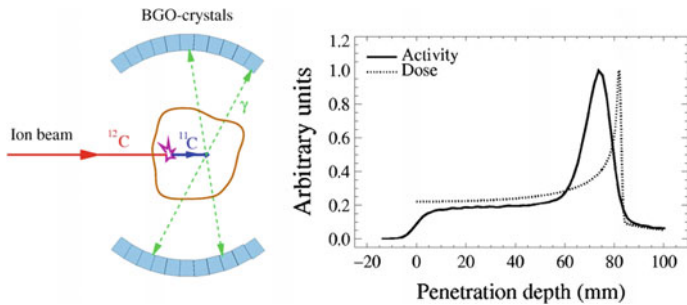


**Fig. 22** Principle of in-vivo and in-situ range verification by PET-techniques [6, 27]. The correlation between depth-dose profile and  $\beta$ -activity distribution is shown in the right part

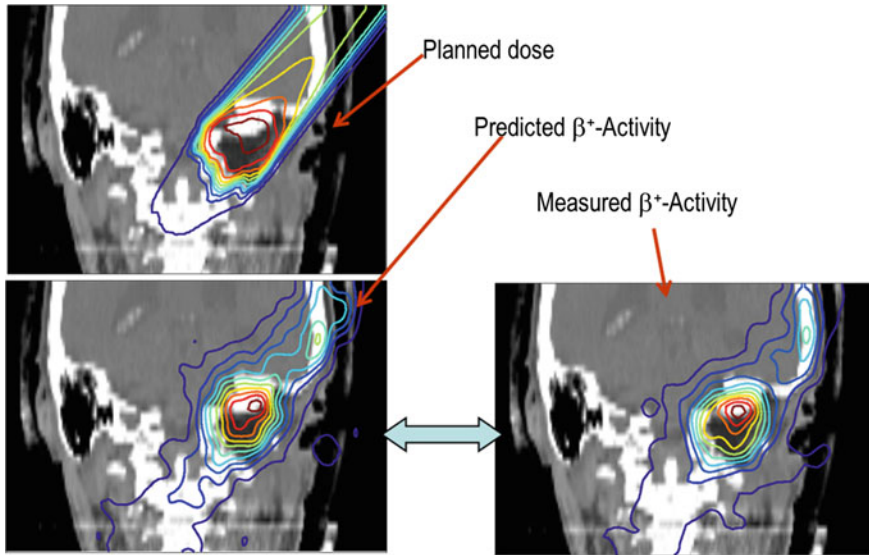


**Fig. 23** Comparison of the measured  $\beta^+$ -activity distribution with the expected distribution calculated on the basis of the treatment plan [6]

irradiation conditions (Fig. 23). Superposition of the measured and calculated  $\beta^+$ -activity distributions then reveals possible differences with an accuracy of about 2–3 mm. This method has proven to be a valuable tool for the quality assurance of heavy-ion therapy and was routinely applied during all patient treatments at GSI.

Optimum performance is obtained with an in-beam PET camera mounted at the patient position as in the pilot project at GSI. In this way, the alteration of the intrinsic spatial  $\beta^+$ -activity distribution by metabolism or blood flow (wash-out effect) can be minimized and the contribution of short-lived positron-emitters like  $^{10}\text{C}$  ( $T_{1/2} = 19\text{ s}$ ) can be fully exploited. On the other hand, space limitations in clinical facilities may not allow mounting a PET camera directly at the irradiation position. In this case PET-verification can be applied off-line by transporting the patient immediately after the treatment session to a PET-system in a neighbouring room and recording the  $\beta^+$ -activity of mainly  $^{11}\text{C}$  ( $T_{1/2} = 20\text{ min}$ ) from a primary  $^{12}\text{C}$  beam. The wash-out effect will then be more pronounced, but the off-beam PET verification can be performed with a full PET-ring which is a great advantage because of the small activity level and generally low counting statistics. The PET verification method can also be applied in proton therapy, but the correspondence between depth-dose distribution (Bragg curve) and the  $\beta^+$ -activity distribution is less favourable for protons as it originates only from target fragments. A comprehensive discussion of in-vivo PET verification with  $^{12}\text{C}$  ions and protons both in-beam and off-beam can be found in [28].

An interesting alternative to the application of PET techniques for in vivo range and dose monitoring in proton- or heavy-ion therapy might be the utilization of *prompt* photon or particle radiation. In fragmentation reactions occurring along the

stopping path of the primary particles prompt photons are emitted by excited nuclei as well as secondary protons,  $\alpha$ -particles, and neutrons which have long ranges and can be detected outside of the patient's body. Since this radiation is emitted promptly, i.e. typically within less than 1 ns after the nuclear reaction, the spatial information is not affected by physiological processes unlike the PET method. As was demonstrated for proton beams of 100–200 MeV stopping in a water phantom, the intensity of prompt photons emitted orthogonally to the beam direction exhibits a peak structure which is correlated with the Bragg peak [24]. In comparison to the  $\beta^+$ -activity distribution shown in Fig. 22, however, the depth profile of the photon emission is much broader and hence the correlation with the Bragg peak position less pronounced. In a recent comprehensive study of prompt gamma yields from stopping proton and carbon ion beams it was found that the gamma yield for carbon ions is about a factor 5 higher than for protons with the same range in water [31]. Extrapolation of these data to real treatment scenarios support the feasibility of prompt-gamma monitoring in particle therapy, but further investigations are needed to evaluate the full potential of this technique.

## 7 Clinical Facilities and Experiences

From 1954 to end of the year 2014 about 137,000 patients were treated with particle therapy, most of them with protons (86 %) and with  $^{12}\text{C}$  ions (14 %) [15]. From the 1980s on the number of patients started to increase significantly from few thousands per year to more than 120,000 per year. In parallel, the number of clinical particle therapy facilities grew up to 48 facilities today. This is an impressive development reflecting the progress in cancer research and particle therapy technology.

At the early stage of particle therapy the treatment irradiations were performed in the experimental environment of nuclear research centres, using particle accelerators which were not optimized for the requirements of particle therapy. The design of clinical facilities, however, has to focus on reliability of the machine operation and extreme care in beam control, which are key issues for operation in a clinical environment and patient safety. From about 1990 on this situation changed when the first dedicated clinical proton therapy facilities came into operation in USA and Japan. Proton therapy is most widely distributed in USA (15 facilities) and Japan (9 facilities).

Considering heavier ions, the BEVALAC (Berkeley/California) for a long time was the only machine worldwide capable of accelerating heavy ions to kinetic energies of several hundred MeV/u as required for radiotherapy. It mainly served as a forefront tool for nuclear physics experiments at high energies. Until its closure (1992) 433 patients were treated with  $^{20}\text{Ne}$  beams. After this exciting pioneering era no more heavy-ion therapy facility was built in USA. In Japan the first dedicated medical heavy-ion therapy facility HIMAC (Heavy Ion Medical Accelerator) at Chiba (Japan) came into operation in 1994. Today Japan is leading in heavy-ion

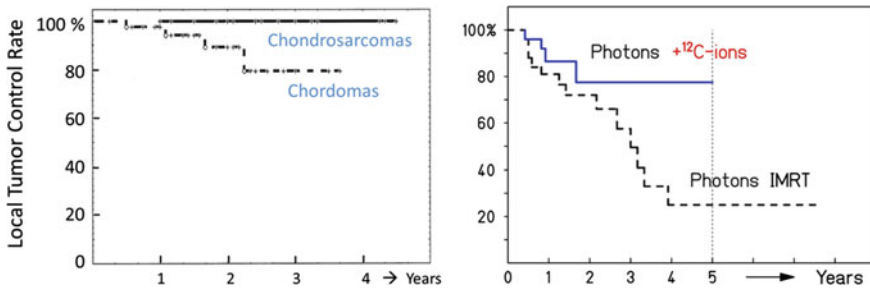


**Fig. 24** Local tumor control rates for patients treated with  $^{12}\text{C}$  ions at GSI Darmstadt (redrawn from [41, 42])

therapy having four facilities in operation and another one (i-Rock, Yokohama) under construction.

While the Japanese particle therapy centres implemented passive beam delivery systems very similar to those developed at Berkeley, two facilities in Europe started to treat patients with new irradiation techniques: PSI (Switzerland) with the ‘spot scanning system’ (1996) and GSI Darmstadt with the ‘raster scanning system’ (1997). Such systems permitted treatments with better conformity of the planned target volume and better sparing of critical structures. The experiences gained in the pilot project at GSI (1997–2008) entered into the construction of the dedicated clinical facility HIT (Heidelberg Ion Therapy) which started patient treatments in 2009. Another heavy-ion facility, the CNAO centre in Pavia (Italy) started patient treatments in 2012, and in Austria the MedAustron facility is expected to start treatments in 2016.

The most important criteria for the clinical assessment of radiation treatment are the tumor control rate, survival rate, side effects and toxicity. Tumor control is commonly defined as the absence of tumor growth up to 5 years after the treatment. Such data can be obtained in clinical studies with patients recruited according to certain selection criteria such as tumor type or tumor site. Some of the first clinical results obtained with  $^{12}\text{C}$  treatments at GSI are shown in Fig. 24.

These data represent the first 152 patients which were treated with  $^{12}\text{C}$  ions at GSI Darmstadt [41]. The patients suffered from slowly growing radio-resistant tumors such as chordomas and chondrosarcomas. Those indications in the skull base were chosen for the first trials because the patient’s head can be immobilized very accurately with full mask techniques. This is important in order to take full advantage of the high precision of dose application in ion therapy. The treatments resulted in 3-year tumor control rates of 100% for chondrosarcomas and 81% for chordomas. The encouraging results were recently confirmed in a long-term study with 10 years follow-up [49]. An example demonstrating the tumor regression in the MRI image is shown in Fig. 25. These first results were comparable or better than those obtained in proton therapy and clearly superior than those known from conventional therapy.

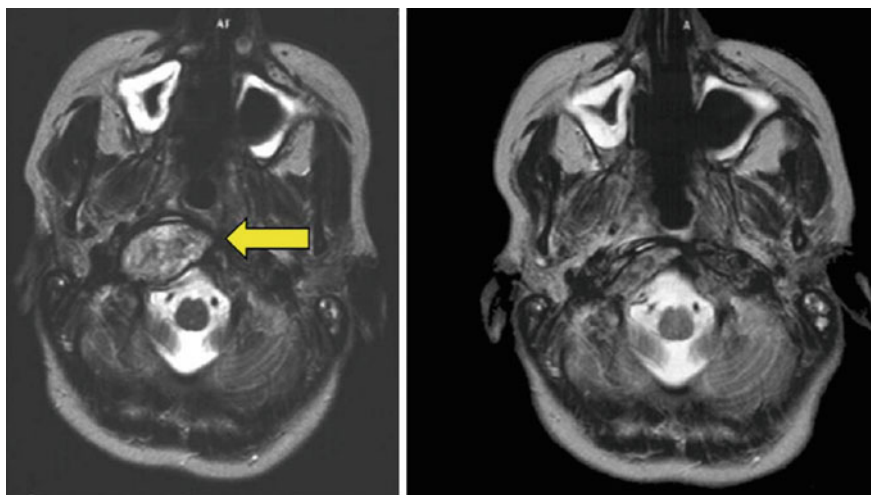


**Fig. 25** Axial MRI scan of a skull base chordoma prior to carbon ion therapy (*left*) and tumor regression 6 weeks after irradiation (*right*) [36]

In the second example shown in Fig. 24 (right part) for adenoid-cystic carcinoma, 29 patients were treated with photon IMRT only and 35 patients treated with photon IMRT and a boost irradiation with  $^{12}\text{C}$  ions. This latter group shows a significant improvement with 77 % tumor control compared to 25 % without carbon boost irradiation [42]. Moreover, much smaller side effects were observed as compared to conventional therapy. Chordoma and chondrosarcoma treatments of young patients (age < 21 y) with  $^{12}\text{C}$  ions (60 GyE total median dose) at GSI were very well tolerated [4].

Many more patients were treated with  $^{12}\text{C}$  ions in Japan (since 1994 more than 10,000 patients). The clinical results confirmed the improved tumor control rates for the tumor types studied at GSI and gave excellent results also for other indications such as prostate, lung and liver tumors [48].

As a result of the promising clinical results obtained in proton and carbon ion therapy, the plans for new clinical centres have recently received a substantial boost [15]. In the near future four large clinical facilities in Europe (HIT Heidelberg, MIT Marburg, CNAO Pavia and MedAustron (Wiener Neustadt)) will offer both proton- and heavy-ion therapy with scanning systems. This will permit meaningful comparisons between proton and heavy ion treatments [50]. Furthermore, treatments with other ions such as  $^4\text{He}$  or  $^{16}\text{O}$  are under preparation at HIT. Helium ions offer higher LET and slightly increased RBE values, but significantly reduced lateral scattering as compared to protons and therefore might be an interesting option. Oxygen ions may be seen as an alternative between carbon and neon ions (used at LBL Berkeley) for the treatment of highly radio-resistant tumors such as glioblastoma.

In proton therapy significant progress was made in the design and construction of very compact superconducting cyclotrons with only few meters diameter. Such

machines, combined with beam scanning and Gantry-system are nowadays available at relatively low cost, facilitating substantially their integration into existing hospital environment.

## References

1. H.W. Barkas, *Nuclear Research Emulsions*, vol. 1 (Academic, New York, 1963)
2. W. Bragg, R. Kleeman, On the  $\alpha$ -particles of radium and their loss of range in passing through various atoms and molecules. *Phil Mag* **10**, 318–340 (1905)
3. N. Bohr, On the theory of the decrease of velocity of moving electrified particles on passing through matter. *Phil. Mag.* **25**, 10–31 (1913)
4. S. Combs et al., Carbon ion radiotherapy for pediatric patients and young adults treated for tumors of the skull base. *Cancer* **115**, 1348–1355 (2009)
5. W.T. Chu et al., Instrumentation for treatment of cancer using proton and light-ion beams. *Rev. Sci. Instrum.* **64**, 2055–2122 (1993)
6. W. Enghardt et al., Charged hadron tumour therapy monitoring by means of PET. *Nucl. Instr. Meth. Phys. Res. A* **525**, 284–288 (2004)
7. K. Gunzert-Marx et al., Secondary beam fragments produced by 200 MeV/u  $^{12}\text{C}$  ions in water and their dose contributions in carbon ion radiotherapy. *New J. Phys.* **10**, 075003 (2008)
8. T. Haberer et al., Magnetic scanning system for heavy ion therapy. *Nucl. Instr. Meth. Phys. Res. A* **330**, 296–305 (1993)
9. E. Haettner et al., Experimental study of nuclear fragmentation of 200 and 400 MeV/u  $^{12}\text{C}$  ions in water for applications in particle therapy. *Phys. Med. Biol.* **58**(23), 8265–8279 (2013)
10. V.L. Highland, Some practical remarks on multiple scattering. *Nucl. Instr. Meth. Phys. Res.* **129**, 497–499 (1975)
11. Y. Hirao et al., Heavy-ion synchrotron for medical use—HIMAC project at NIRS Japan. *Nucl. Phys. A* **538**(1992), 541c–550c (1992)
12. ICRU, ICRU Report 78. Prescribing, recording and reporting proton-beam therapy. *J. ICRU* **7**(2) (2007)
13. O. Jäkel, in *Radiotherapy with Protons and Ion Beams*, ed. by C. Alonso, M.V. Andrés, J. García-Ramos, F. Pérez-Bernal. La Rábida 2009 International Scientific meeting on Nuclear Physics, AIP Conference Proceedings 1231 (2009)
14. A.D. Jensen et al., COSMIC: A regimen of intensity modulated radiation therapy plus dose-escalated, raster-scanned carbon ion boost for malignant salivary gland tumors: results of the prospective phase 2 trial. *Int. J. Radiat. Oncol. Biol. Phys.* **93**(1), 37–46 (2015)
15. M. Jermann, Particle therapy statistics in 2013. *Int. J. Part. Ther.* **1**, 40–43 (2014)
16. B. Jones, Towards achieving the full clinical potential of proton therapy by inclusion of LET and RBE models. *Cancers* **7**, 460–480 (2015)
17. C.P. Karger et al., A system for three-dimensional dosimetric verification of treatment plans in intensity-modulated radiotherapy with heavy ions. *Med. Phys.* **26**, 2125–2132 (1999)
18. G. Kraft, Tumor therapy with heavy charged particles. *Prog. Part. Nucl. Phys.* **45**, S473–S544 (2000)
19. M. Krämer, Calculations of heavy-ion track structure. *Nucl. Instr. Meth. Phys. Res. B* **105**, 14–20 (1995)
20. M. Krämer et al., Treatment planning for heavy-ion radiotherapy: Physical beam model and dose optimization. *Phys. Med. Biol.* **45**, 3299–3317 (2000)
21. M. Krämer, M. Scholz, Treatment planning for heavy-ion radiotherapy: calculation and optimization of biologically effective dose. *Phys. Med. Biol.* **45**, 3319–3330 (2000)
22. M. Krämer et al., Biological dosimetry of complex ion radiation fields. *Phys. Med. Biol.* **48**, 2063–2070 (2003)

23. N. Matsufuji et al., Relationship between CT number and electron density, scatter angle and nuclear reaction for hadron-therapy treatment planning. *Phys. Med. Biol.* **43**, 3261–3275 (1998)
24. C.H. Min et al., Determination of distal dose edge location by measuring right-angled prompt-gamma rays from a 38-MeV proton beam. *Nucl. Instrum. Meth. Phys. Res. A* **580**, 562–565 (2007)
25. G. Molière, Theorie der Streuung schneller geladener Teilchen II, Mehrfach- und Vielfachstreuung. *Z. Naturforsch.* **3a**, 78–97 (1948)
26. H. Paganetti et al., Relative biological effectiveness (RBE) values for proton beam therapy. *Int. J. Radiat. Oncol. Biol. Phys.* **53**, 407–421 (2002)
27. K. Parodi et al., Experimental study on the feasibility of in-beam PET for accurate monitoring of proton therapy. *IEEE Trans. Nucl. Sci.* **52**, 778–786 (2005)
28. K. Parodi et al., Comparison between in-beam and offline positron emission tomography imaging of proton and carbon ion therapeutic irradiation at synchrotron- and cyclotron-based facilities. *Int. J. Radiat. Oncol. Biol. Phys.* **71**, 945–956 (2008)
29. E. Pedroni et al., The 200-MeV proton therapy project at the Paul Scherrer Institute: conceptual design and practical realization. *Med. Phys.* **22**, 37–53 (1995)
30. P.L. Petti, A.J. Lennox, Hadronic radiotherapy. *Ann. Rev. Nucl. Part. Sci.* **44**, 155–197 (1994)
31. M. Pinto et al., Absolute prompt-gamma yield measurements for ion beam therapy monitoring. *Phys. Med. Biol.* **60**, 565–594 (2015)
32. M.R. Raju, Advances in hadrontherapy, International Congress Series No. 1077 (Elsevier Science, New York, 1994), pp. 67–79
33. E. Rietzel et al., Range accuracy in carbon ion treatment planning based on CT-calibration with real tissue samples. *Radiat. Oncol.* **2**, 14 (2007)
34. B. Schaffner, E. Pedroni, The precision of proton range calculations in proton radiotherapy treatment planning: experimental verification of the relation between CT-HU and proton stopping power. *Phys. Med. Biol.* **43**, 1579–1592 (1998)
35. J.M. Schippers et al., The SC cyclotron and beam lines of PSI's new proton therapy facility PROSCAN. *Nucl. Instr. Meth. Phys. Res. B* **261**, 773–776 (2007)
36. D. Schardt et al., Heavy-ion tumor therapy: Physical and radiobiological benefits. *Rev. Mod. Phys.* **82**, 383–425 (2010)
37. M. Scholz, Effects of ion radiation on cells and tissues. *Adv. Polym. Sci.* **62**, 96–155 (2003)
38. M. Scholz et al., Computation of cell survival in heavy ion beams for therapy. The model and its approximation. *Radiat. Environ. Biophys.* **36**, 59–66 (1997)
39. M. Scholz, G. Kraft, Calculation of heavy ion inactivation probability based on track structure, X-ray sensitivity and target size. *Radiat. Prot. Dosim.* **52**, 29–33 (1994)
40. E. Schrödinger, *What is Life?* (Cambridge University Press, Cambridge, 1944)
41. D. Schulz-Ertner et al., Results of carbon ion radiotherapy in 152 patients. *Int. J. Radiat. Oncol. Biol. Phys.* **58**, 631–640 (2004)
42. D. Schulz-Ertner et al., Therapy strategies for locally advanced adenoid cystic carcinomas using modern radiation therapy techniques. *Cancer* **104**, 338–344 (2005)
43. D. Schulz-Ertner et al., Effectiveness of carbon ion radiotherapy in the treatment of skull-base chordomas. *Int. J. Radiat. Oncol. Biol. Phys.* **68**, 449–457 (2007)
44. R. Serber, Nuclear reactions at high energies. *Phys. Rev.* **72**(11), 1114–1115 (1947)
45. L. Sihver et al., Depth-dose distributions of high-energy carbon, oxygen and neon beams in water. *Jpn. J. Med. Phys.* **18**(1), 1–21 (1998)
46. C.A. Tobias, Heavy charged particles in cancer therapy. *Radiobiology and Radiotherapy, Institute Monograph No. 24* (1967)
47. Y.S. Tsai, Pair production and bremsstrahlung of charged leptons. *Rev. Mod. Phys.* **46**, 815–851 (1974)
48. H. Tsujii et al., Clinical advantages of carbon-ion radiotherapy. *New. J. Phys.* **10**, 075009 (2008)
49. M. Uhl et al., High control rate in patients with chondrosarcoma of the skull base after carbon ion therapy: first report of long-term results. *Cancer* **120**(10), 1579–1585 (2014a)
50. M. Uhl et al., Comparing the use of protons and carbon ions for treatment. *Cancer J.* **20**(6), 433–439 (2014b)

51. R.R. Wilson, Radiological use of fast protons. *Radiology* **47**, 487–491 (1946)
52. W.K. Weyrather et al., RBE for carbon track-segment irradiation in cell lines of differing repair capacity. *Int. J. Radiat. Biol.* **75**, 1357–1364 (1999)
53. R.R. Wilson, *Advances in Hadrontherapy*, International Congress Series No. 1144, (Elsevier Science, New York, 1997), pp. ix–xiii



Basic Concepts in Nuclear Physics: Theory, Experiments  
and Applications

2015 La Rábida International Scientific Meeting on  
Nuclear Physics

García-Ramos, J.-E.; Alonso, C.E.; Andrés, M.V.;  
Pérez-Bernal, F. (Eds.)

2016, XXXI, 234 p. 148 illus., 119 illus. in color.,  
Hardcover

ISBN: 978-3-319-21190-9